Dense colloidal fluids form denser amorphous sediments

Shir R. Liber[a,b], Shai Borohovich[a,b], Alexander V. Butenko[a,b], Andrew B. Schofield[c], and Eli Sloutskin[a,b,1]

[a]Physics Department and [b]Institute for Nanotechnology and Advanced Materials, Bar-Ilan University, Ramat-Gan 52900, Israel; and [c]School of Physics and Astronomy, University of Edinburgh, Edinburgh EH9 3JZ, United Kingdom

Edited by David A. Weitz, Harvard University, Cambridge, MA, and approved February 25, 2013 (received for review August 29, 2012)

We relate, by simple analytical centrifugation experiments, the density of colloidal fluids with the nature of their randomly packed solid sediments. We demonstrate that the most dilute fluids of colloidal hard spheres form loosely packed sediments, where the volume fraction of the particles approaches in frictional systems the random loose packing limit, $\varphi_{RLP} = 0.55$. The dense fluids of the same spheres form denser sediments, approaching the so-called random close packing limit, $\varphi_{RCP} = 0.64$. Our experiments, where particle sedimentation in a centrifuge is sufficiently rapid to avoid crystallization, demonstrate that the density of the sediments varies monotonically with the volume fraction of the initial suspension. We reproduce our experimental data by simple computer simulations, where structural reorganizations are prohibited, such that the rate of sedimentation is irrelevant. This suggests that in colloidal systems, where viscous forces dominate, the structure of randomly close-packed and randomly loose-packed sediments is determined by the well-known structure of the initial fluids of simple hard spheres, provided that the crystallization is fully suppressed.

amorphous solids | colloids | microscopy | glass | granular matter

Physical mechanisms that determine structure and density of noncrystalline solids remain controversial after several decades of intense experimental (1–6) and theoretical (7–10) research. In granular systems of hard spheres, for a wide range of experimental and theoretical protocols, particle motion is arrested or "jammed" when the volume fraction of the spheres reaches $\varphi_{RCP} \approx 0.64$, known as the random close packing (RCP) density. However, the notion of random close packing is ill-defined; denser packings, up to the limit of ~0.7405, are readily achieved by increasing the crystallinity of the structure, whereas the randomness of the RCP state must still be quantified (11). Moreover, some experiments (12–14) and simulations (15, 16) indicate that the system can become solid-like at a much lower volume fraction, down to the so-called random loose packing (RLP) limit of $\varphi_{RLP} \approx 0.55$. In particular, experimental packings of macroscopic spheres, gently sedimented in a buoyancy-matched fluid, closely approach the RLP limit (13, 17, 18). The RLP limit, related to the friction between the constituent particles (14, 16), is even more controversial than the RCP (11, 17). Thus, the notion of both the RLP and the RCP states remains ill-defined (11, 19).

We form sediments out of a fluid suspension of hard micrometer-sized spheres in a solvent, known as colloids, and demonstrate that the structure of the initial fluid uniquely determines the density of the sediments. This is the case for a wide range of sedimentation rates, which are sufficiently high to prohibit crystallization. In particular, the most disordered suspensions, where the initial volume fraction φ_0 tends to zero, form loosely packed sediments; the volume fraction of these sediments φ_j approaches φ_{RLP}. Denser suspensions form denser sediments, where φ_j approaches φ_{RCP}. The structure of fluids of simple hard spheres in thermodynamic equilibrium, such as our initial colloidal suspensions, is well established (20). Therefore, the observed relationship between the structure of these simple fluids and the density of their nonergodic sediments suggests that the thermodynamics of the initial fluids may possibly be used to fully understand the physics of the RLP and the RCP states in amorphous sediments. This deeper understanding of sediments, in addition to its fundamental importance, may contribute to abundant industrial processes, such as the slip-casting (21) of ceramics, in which water is rapidly drawn from a suspension of clay particles to form solid ceramic objects.

Materials and Methods

To form the sediments, we suspend poly(methyl methacrylate) (PMMA) colloidal spheres in mixed decahydronaphthalene (≥98%; Sigma-Aldrich). The sediment is formed by centrifugation in a thermally regulated centrifuge (Advanced LF-110 LUMiFuge), with the amplitude of the centrifugal acceleration $\vec{a}$ set to a value between 130g and 2,080g, where $g = 9.8$ m/s^2. We use direct confocal microscopy, in three dimensions, to measure the radial distribution function of the colloids (20) $g(r)$ and the crystalline local bond-order parameters (11); these metrics confirm absence of any significant crystalline domains within the sediments. The particles are sterically stabilized by poly-12-hydroxystearic acid (22), such that the interactions in a fluid suspension are best described by a hard potential (23, 24). The dynamic viscosity of our solvent at $T = 22$°C, obtained using a Cannon-Manning semimicro viscometer, is $\eta_s = 2.4 \pm 0.05$ mPa·s. The average diameter of our particles is $\sigma = 2.4 \pm 0.05$ μm and their polydispersity is <5%, as detected by static and dynamic light scattering, confocal microscopy, and scanning electron microscopy of dry particles under vacuum; this very low polydispersity of our particles allows any variation in the density of the sediments due to possible segregation of particle sizes to be ruled out completely. The diameter of our particles is sufficiently small so that the particles undergo Brownian motion. The time for a free particle in a solvent to diffuse its own diameter is $t_D = (2k_BT)^{-1}\pi\sigma^3\eta_s = 12.8$ s at $a = 130g$; this time scale corresponds to a free particle displacement of ~1 mm along the effective gravity, so thermal structural reorganization of solid sediments during the centrifugation is unlikely.

All our samples are prepared by dilution (or removal of supernatant) from the same initial batch of suspension; the volume fraction of colloids in this batch φ_{00} was initially estimated as 0.3–0.4. The sample is homogenized and randomized by vortex mixing after either dilution or removal of the supernatant. With the gravimetric density of our solvent $\rho_s = 0.868$ g/cm^3 measured by pycnometry, the volume fractions of all our samples, as a function of φ_{00}, are known to a high precision. We use analytical centrifugation to obtain the value of φ_{00}, as detailed below. About 0.4 mL of the suspension is loaded into an optically transparent polyamide cell, which has a rectangular cross-section of 2 × 8 mm, so that the initial height of the sample is $L_0 \approx 25$ mm. The cell is then vigorously shaken on a vortexer and placed into the centrifuge (Fig. 1 *Inset*). Our LUMiFuge analytical centrifuge measures light transmission

Author contributions: A.V.B. designed research; S.R.L., S.B., and A.V.B. performed research; A.B.S. contributed new reagents/analytic tools; S.R.L., S.B., A.V.B., and E.S. analyzed data; and A.V.B. and E.S. wrote the paper.

The authors declare no conflict of interest.

This article is a PNAS Direct Submission.

[1]To whom correspondence should be addressed. E-mail: eli.sloutskin@biu.ac.il.

This article contains supporting information online at www.pnas.org/lookup/suppl/doi:10.1073/pnas.1214945110/-/DCSupplemental.

*We interpolate the experimental $\eta(\varphi_0)/\eta_s$ [Segrè PN, Meeker SP, Pusey PN, Poon WCK (1995) Viscosity and structural relaxation in suspensions of hard-sphere colloids. *Phys Rev Lett* 75(5):958–961] by $[A/(A - \varphi_0)]^\alpha$, where $A = 0.53$ and $\alpha = 1.53$, which perfectly matches the experimental data up to $\varphi_0 = 0.45$.

†The Reynolds and Stokes numbers (14) in our experiments are very low, below 3×10^{-4} and 4×10^{-5}, respectively. Thus, compaction mechanisms discussed by Farrell et al. (14) are irrelevant in our case; in our range of parameters, particles entering the packing do not have the ability to rearrange the structure of the packing. The Péclet number (5) ranges in our studies from 10 to 10^3.

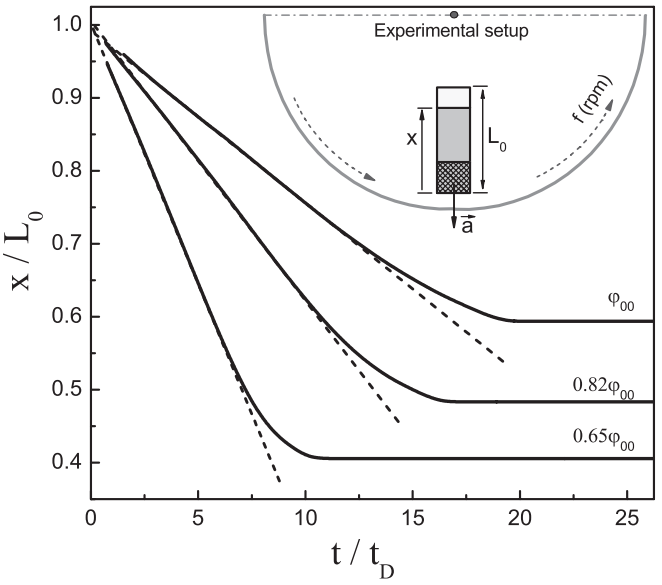

Fig. 1. The front positions x separating the colloid-free solvent and the sedimenting suspension exhibit a linear dependence on time, at early centrifugation times. This indicates that the sedimentation velocity is constant, as for an individual sphere in a solvent; then, a sharp transition is observed, as all colloids become fully arrested in the solid sediment. Here $|\vec{a}| = 1,170\,g$ and $t_D = 12.8$ s is the Brownian self-diffusion time of our particles. Linear fits to the data are shown in dashes. (*Inset*) A top view of our sample, rotated at a frequency f in a centrifuge. The sediment is shown in a check pattern, the fluid colloidal suspension in gray, and the supernatant in white. The interface between the sedimenting colloidal suspension and the supernatant is at a distance x from the bottom of the cell.

profiles through the sample (*Supporting Information*) at a wavelength of 870 nm, in situ, during the centrifugation.

Results

To accurately calibrate the volume fraction of particles in the suspensions, we measure the velocity of colloidal sedimentation (25). As the particles sediment, a colloid-free region (supernatant) is formed in the topmost part of the sample, as shown in Fig. 1 *Inset*. We track the position x of the boundary between the supernatant at the top of the sample and the fluid colloidal suspension below. First, $x(t)$ is linear in time; then, it saturates when all of the particles are fully arrested within the sediment, as shown in Fig. 1. Interestingly, the linear regime survives even for the densest suspensions, during most of the centrifugation process, indicating that the densities and the structures of our fluid suspensions do not significantly change during the centrifugation. Although significant spatial fluctuations in microscopic sedimentation velocities of the particles were previously observed in similar systems (26), these fluctuations do not necessarily change the structure of the suspensions. Indeed, the fluctuations were interpreted in the past in terms of an effective temperature (26); in our system of hard spheres the energy scale is missing, such that the average structure of the fluid does not depend on the temperature. The slope of the linear region of $x(t)$ in Fig. 1 yields the velocity of the sedimentation front $v = dx/dt$. For a very dilute suspension, v is determined by the simple Stokes' law. At high concentrations of colloids, front velocities are slowed by interparticle interactions that increase the fluid drag acting on each colloidal sphere.

To focus on the hydrodynamics of our fluids, we divide our front velocities, obtained in the linear range of $x(t)$, by the amplitude of the centripetal acceleration $a = (2\pi f)^2 R$, where R and f are the radius and the frequency of rotation in the centrifuge, respectively. For Stokesian sedimentation of a sphere in a fluid, its velocity is $v_0 = \Delta\rho\sigma^2 a/(18\eta_s)$, where $\Delta\rho = \rho_p - \rho_s$ is the mismatch between the density of the sphere ρ_p and that of the surrounding fluid ρ_s, which has a dynamic viscosity η_s; thus, for a given sphere in a given fluid, v_0/a is constant. Similarly, all our front velocities $v(\varphi_0)$ collapse together, when normalized by the corresponding values of a, as shown in Fig. 2. The collapse of the data is quite remarkable, given that the amplitudes of our $\vec{a}$ vary by a factor of 16 and the average separation between the particles in the fluid at $\varphi_0 \approx 0.35$ is only 1.5σ. With the v/a collapsed together, we can describe our front velocity by the Stokes formula for the velocity of an individual sphere, as above, where η_s and ρ_s are replaced by the viscosity η and the density ρ of the suspension. Importantly, these η and ρ now depend on the volume fraction of colloids φ_0. To match this effective medium approximation to our experimental data, we use the experimental static $\eta(\varphi_0)$ and directly measure the density of our suspensions ρ by pycnometry, so that $\rho_p = \varphi_0^{-1}[\rho_s(1-\varphi_0) - \rho]$.* This allows our experimental v/a, for a wide range of centrifugation rates and volume fractions, to be matched, with the only free-fitting parameter being φ_{00}. Note the very nice fit to the experimental data, as shown by a dashed curve in Fig. 2, with a fitted value of $\varphi_{00} = 0.35$. The fitted φ_{00} allows the ρ_p value to be obtained as 1.045 g/cm^3, which is smaller than the bulk density of solid PMMA (27) (1.17–1.20 g/cm^3), yet significantly denser than $\rho_s = 0.868$ g/cm^3 of the pure solvent, indicating that some absorbtion of decahydronaphthalene into the particles may have possibly occurred. Most importantly, the obtained value of φ_{00} allows the absolute φ_0 values to be known with a high accuracy, such that the volume fraction φ_j of colloids within the sediments is obtained as $\varphi_j = \varphi_0 L_0/x(t \to \infty)$.

A very common, yet questionable (25), assumption in colloidal physics is that the particle volume fraction in sediments prepared by centrifugation is $\varphi_j = \varphi_{RCP} \approx 0.64$. In particular, φ_j is typically assumed to be independent of the colloidal volume fraction in the initial suspension (25). This assumption was questioned in recent experimental (28) and theoretical (29) studies, demonstrating a decrease in φ_j with φ_0 in packings of macroscopic objects. However, in these studies the inertial forces were significant. Our sediments are prepared at low Reynolds numbers, typical for colloidal systems, where the inertial effects are negligible.† Strikingly, the measured colloidal volume fractions of our sediments increase with the density of the initial fluid suspensions, as shown in Fig. 3*A* (solid symbols). The measured φ_j are independent of the initial height L_0 of the suspension (Fig. 3*B*). This indicates that the potential energy of our colloids with respect to gravity is irrelevant. In addition, this demonstrates that φ_j are not sensitive to the macroscopic shape of the top of the sediment, as also to the density of particles in the topmost region of the sediment, which is formed in the nonlinear regime of $x(t)$ (Fig. 1). The measured φ_j are also independent of the centripetal acceleration, in our range $130g < a < 2{,}080g$, which corresponds to Péclet numbers ranging from 10 to 10^3. The independence of φ_j on a and L_0 stays in contrast with the fluidized bed experiments (12, 30), where a packing of granular spheres is fluidized by multiple water flow pulses, followed by formation of a new solid packing. In the fluidized bed experiments, the densities of solid packings decrease monotonically with the flow rate, so that the most expanded fluidized beds form highly expanded solid packings. Unfortunately, the volume fraction of the fluidized beds was not measured and the homogeneity of the fluidized state was not tested; this and the dependence of these results, obtained at Reynolds numbers of order unity, on sample height and on the rate of sedimentation (12, 30) complicates the comparison with our work, motivating additional studies in both fields.

We confirm the increase of φ_j with φ_0, observed in Fig. 3*A*, independently, by measuring the mass of the supernatant in some of these samples. The observed scaling of φ_j with φ_0 in our system allows the density of our packings to be tuned in a controllable way. This is impossible with the classic granular packings (1, 18), where various, rather uncontrolled tapping protocols

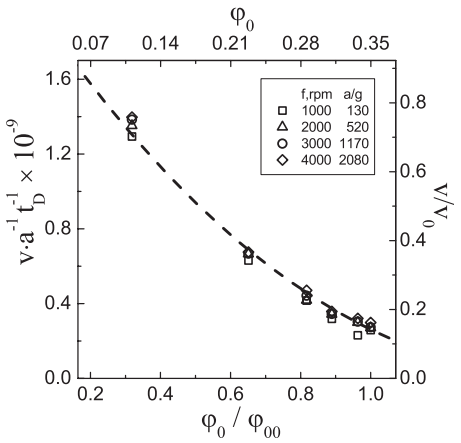

Fig. 2. To collapse together the data obtained at different centrifugation rates (see legend), the experimental sedimentation front velocities $v = dx/dt$ are scaled by the amplitude of centripetal acceleration a (left y axis) or, equivalently, by the velocity v_0 of a free colloidal sphere at the corresponding a (right y axis). Our φ_0 are very accurately known as a function of the volume fraction of the initial suspension φ_{00}, which is then diluted. However, our accuracy in determining the φ_{00} value itself is not so high; thus, we set φ_{00} as a free-fitting parameter. Note the perfect match between the effective medium theory (dashes) and the experimental data (symbols), where φ_{00} is the only tunable parameter. The fitted value of φ_{00} allows the absolute φ_0 values (scale on the top) to be obtained.

were used to increase the packing density (17). Importantly, our experimental φ_j tend to 0.55 for the most dilute suspensions, where $\varphi_0 \to 0$. This value is very close to the well-known, yet highly controversial, RLP limit of the granular packings (13, 14, 16–18). Moreover, a sediment can never be less dense than the original suspension, $\varphi_j > \varphi_0$; thus, all our data must fall above the $\varphi_j = \varphi_0$ dashed-and-dotted line in Fig. 3*A*. This obvious geometrical argument implies that there must be an upper limit on the density of amorphous colloidal sediments, set by the intersection between the experimental $\varphi_j(\varphi_0)$ scaling (fitted by a solid line) and the $\varphi_j = \varphi_0$ dashed-and-dotted line. This limiting volume fraction is obtained as $\varphi_j = 0.64$, which is very close to the well-known, yet strongly debated, RCP limit (11). The observed $\varphi_j(\varphi_0)$ in our system, where Péclet numbers are sufficiently high so that structural thermal relaxation within the solid sediments is prohibited, suggests that the states of our solid sediments may possibly be related to the thermodynamics of the initial fluids.

Discussion

To test the relation between the density of the sediments and the thermodynamic states of the initial fluids of hard spheres, we carry out simple computer simulations, where we neglect the hydrodynamic interactions and any possible structural reorganizations within the sediments and within the fluid suspensions. We choose these, somewhat oversimplified, conditions to focus on the most basic physical mechanisms underlying the experimental $\varphi_j(\varphi_0)$ scaling. We simulate a fluid of simple hard spheres, thermodynamically equilibrated at an initial volume fraction φ_0. As mentioned earlier, the velocity fluctuations in experimental sedimenting suspensions, while raising the effective temperature of the suspension (26), do not necessarily alter the sample-averaged local structure in our fluids of hard spheres with respect to the thermally equilibrated structure, which is dictated solely by the entropy and therefore does not depend on the temperature. Therefore, modeling the structure of our sedimenting fluid suspensions by that of a thermodynamically equilibrated fluid is a reasonable approximation. The simulated cell, where the number of particles was chosen to be between 4×10^3 and 4×10^5, is subject to periodic boundary conditions in x and y directions. To simulate the structure of the sediment, we make the particles fall, one by one, along the $-z$ direction, to the bottom of the cell ($z = 0$). The particles that are the closest to the bottom are the first to fall. To stop falling, the particle must either contact the bottom of the cell or contact Z_s particles that already belong to the sediment. If $Z_s > 1$, once a falling particle meets its first contact with a sphere belonging to the sediment, it slides along the circumference of that sphere; then it either meets another contact or falls again (*Supporting Information*). Once it has stopped falling, the particle is considered to belong to the sediment; its position is then fixed during the rest of the simulation. Importantly, the sedimentation process is nonrandom, such that for a given structure of the initial fluid, the structure of the final sediment is fully determined. Surprisingly for such a simplistic simulation, the densities of our simulated sediments increase (roughly) linearly with φ_0 (Fig. 4*A*), as in the experiments. The slope of the simulated $\varphi_j(\varphi_0)$ varies with the number of supports Z_s, which are necessary to stabilize a particle under gravity. By symmetry, if a particle is supported on average by Z_s underlying particles, it must support (on average) Z_s overlying particles. The data in Fig. 4*A* are labeled by the total number of contacts per particle $Z = 2Z_s$ in each of the simulations. When the number of contacts is low $Z = 2$, the sediments are very dilute. This is the case with the sediments of cohesive particles (18) and packings prepared by random ballistic deposition (31) of sticky spheres. In these systems (31), $\varphi_j \simeq 0.15$ for $\varphi_0 = 0$, in perfect agreement with our simulations. For frictionless spheres at the isostatic conditions, the number of contacts is $Z = 6$ and the slope of $\varphi_j(\varphi_0)$ is very low (15). We show the slopes of the simulated $\varphi_j(\varphi_0)$ in Fig. 4*B* (open symbols), where the values decay exponentially with Z. The slope of the experimental data is consistent with the number of contacts being (slightly smaller than) ~4, as in an isostatic frictional system, where the spheres are unable to slip past each other. Whereas our colloids behave as perfect hard spheres in their fluid state, the friction in colloidal systems is difficult to obtain by experimental techniques (5). However, the arrested rotational diffusion in our

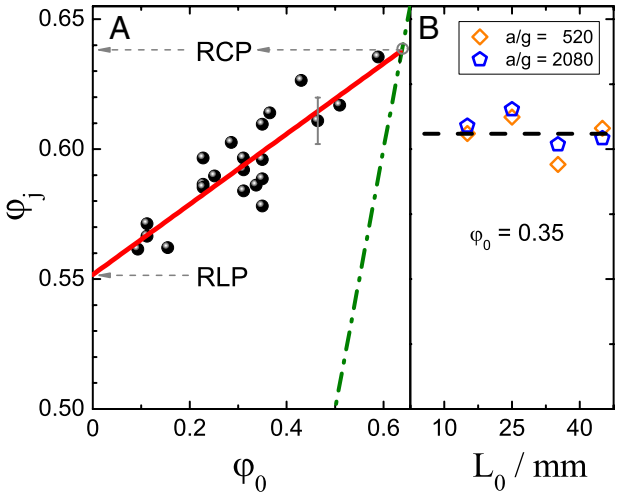

Fig. 3. (*A*) The experimental volume fraction of the spheres in the sediment φ_j increases with their volume fraction within the initial suspension φ_0. The denser suspensions are less disordered, such that they pack to a higher density. A linear fit (solid line) to our experimental data (symbols) tends to $\varphi_{RLP} \approx 0.55$ for the most disordered initial suspensions ($\varphi_0 \to 0$); it intersects the (dashed-and-dotted) $\varphi_j = \varphi_0$ line at $\varphi_j = \varphi_{RCP} = 0.64$, setting the limit on the possible density of sediments in our simple system of hard spheres. The φ_j do not vary within our range of $|\vec{a}|$; the solid symbols are the averages for different $|\vec{a}|$. The estimated error bar is shown on the right. (*B*) The measured $\varphi_j(\varphi_0 = 0.35)$ data are independent of the height L_0 of the initial fluid suspension.

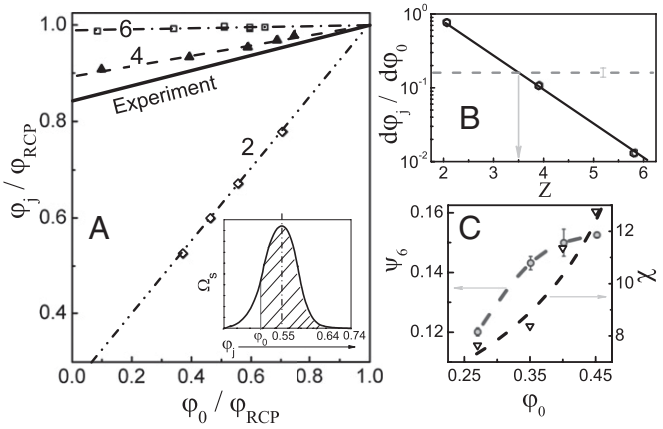

Fig. 4. (*A*) The densities of simulated sediments (symbols) depend linearly on the volume fraction of the spheres in the initial suspension, reproducing the experimental dependence (solid line). Both *x* axis and *y* axis are normalized to have all datasets pass through (1, 1). The average number of contacts per particle Z is indicated for each of the simulated data sets. (*Inset*) Schematic behavior of $\Omega_s(\varphi_j)$. Only those states that belong to the hatched region of $\Omega_s(\varphi_j)$ can form from a fluid at φ_0. (*B*) The slopes of the data from *A* exhibit a linear dependence on the number of contacts per particle Z. The slope of the experimental $\varphi_j(\varphi_0)$ is plotted by a horizontal dashed line, suggesting that the experimental particles have on average $Z \approx 3.5$ contacts per particle. (*C*) Positional correlations $\chi = \int_0^{7\sigma} (g(r)-1)^2 r^2 dr$ between experimental colloids (triangles) are stronger for sediments formed from denser initial fluids. Similarly, the excess bond-orientational order with respect to that in an ideal gas ψ_6, shown in circles, increases with φ_0 of the initial fluid.

sediments (*Supporting Information*) suggests that the frictional forces between the particles may be significant, in agreement with the obtained value of Z. Although direct measurement of contacts between the colloids is a very challenging task, the simulated coordination numbers are in good agreement with the experimental ones, for all φ_j (*Supporting Information*).

Our simulations, where structural relaxation is prohibited and the sedimentation process is deterministic, link between the structures of solid sediments and the fluid states of initial suspensions: Each fluid state, specified by the position of all particles in the simulation, forms a sediment with a certain predetermined structure. When the initial fluid is very dilute ($\varphi_0 \to 0$) and the correlations between particles are negligible, all mechanically stable structures of sediments are equally probable. The number of different mechanically stable structures varies with the sediment density φ_j, peaking (11) for the frictional particles (32) at $\varphi_j \approx 0.55$ (Fig. 4*A Inset*). However, by simple geometry, when φ_0 is finite, the only states of the sediment that can form are the ones that are denser than the initial fluid, $\varphi_j > \varphi_0$ (Fig. 4*A Inset*, hatched area). This shifts the average density of the sediment to a higher value of φ_j, as experimentally observed.

To test the physical mechanism for $\varphi_j(\varphi_0)$ dependence, we measure the degree of structural order within the colloidal sediments formed from fluids of different φ_0, using direct confocal microscopy. The degree of structural order χ is quantified by the deviation of the experimental radial distribution functions from their value for an ideal gas $g(r) = 1$, where correlations are missing. The value of χ increases for sediments prepared from denser fluids, as demonstrated in Fig. 4*C*, indicating that sediments prepared from denser fluids are more ordered (*Supporting Information*). Whereas χ measures the positional order of the particles, which has a complex dependence on φ_j, another measure of structural order is provided by the orientations of geometrical bonds between the particles. The excess of this bond-orientational order with respect to an ideal gas is given by $\psi_6 = \langle q_{ij} \rangle - \langle q_{ij}^{IG} \rangle$, where averaging is carried out over the whole sample and $q_{ij} = q_{ii}^{'-1} \sum_{m=-6}^{6} \tilde{q}_m(i) \tilde{q}_m^*(j)$ is the correlation between bond orientations of the i-th and the j-th particles, normalized by $q_{ii}^{'} = \sum_{m=-6}^{6} \tilde{q}_m(i) \tilde{q}_m^*(i)$ to have the correlation of the i-th particle with itself be identically equal to unity. The definition of q_{ij} makes use of the sixfold-symmetric local bond-orientational parameter of the i-th particle $\tilde{q}_m(i) = \sum_{k \in \{NN\}} Y_6^m(i,k)$, where $Y_6^m(i,k)$ are the spherical harmonics (of degree 6 and order m) for the orientation of the bond between the i-th particle and the k-th one; the k-index summation is carried out over all nearest neighbors of the i-th particle. With this definition of q_{ij}, which was widely used in many previous studies (33, 34), the $\langle q_{ij} \rangle$ does not completely vanish even in a fluid or in an ideal gas; therefore, we measure the excess orientational correlation ψ_6, where the ideal gas value $\langle q_{ij}^{IG} \rangle$ is subtracted. The resulting ψ_6 values increase for those sediments that were formed from high-density fluids, as shown in circles in Fig. 4*C*; thus, both the bond-orientational order and the positional order indicate that sediments formed by denser fluids are more ordered, suggesting that microscopic low-density states are excluded in these sediments.

In our range of Péclet numbers, crystallization is prohibited and the sediment structure is amorphous. The number of amorphous sediment states drops at very high φ_j, as for the uniformly compressed systems at the jamming transition (7, 35); this possibly sets the highest limit for the density of fluids and amorphous sediments in colloidal suspensions, denoted above by φ_{RCP}. Clearly, a more elaborate theoretical model is necessary to fully account for the details of our experimental and simulated observations.

In addition to structural measurements, we demonstrate that sediments prepared from dense colloidal fluids exhibit higher mechanical stability. We prepare three sediments from three initial suspensions, which are identical except for having different φ_0. We choose the amounts of the initial suspensions such that the heights of these three sediments are identical; supernatant is added, where needed, after the formation of the sediment, to equalize the total height of the three samples. We compare the mechanical stability of these three sediments by placing them horizontally on a vortex mixer. After a couple of minutes, the sediment that was prepared from a low-φ_0 fluid is almost completely molten, whereas the sediment that was prepared from a high-φ_0 fluid is almost intact (see the relative heights of the sediments in Fig. 5). Similar observations were previously reported for the macroscopic fluidized bed packings (36), which suggests that these results may have an important impact on abundant processes based on sedimentation, in nature (37) and industry.

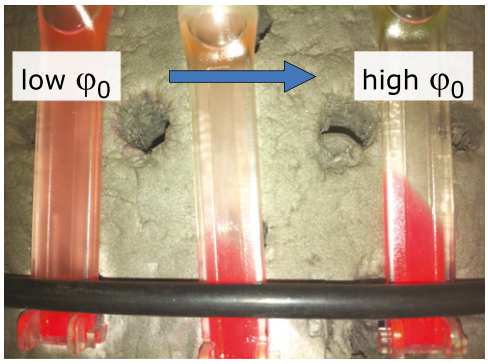

Fig. 5. Three cuvettes, with colloidal sediments inside, on top of the vortex mixer. The image was taken a couple of minutes after the beginning of mixing. The initial sediments were prepared to have the same height, such that the height difference between the sediments in the image measures the mechanical stability of these sediments under vortexing. The sample on the left, which was prepared from a low-φ_0 fluid, is almost completely molten. The sample on the right, which was prepared from a high-φ_0 fluid, is almost intact. This indicates that the denser colloidal fluids form sediments that are not only denser but also mechanically more stable.

Preliminary results (22) suggest that the observed $\varphi_j(\varphi_0)$ scaling is not unique for systems of sterically stabilized colloids. The same type of behavior takes place for other types of colloids, for example for 400-nm, charge-stabilized silica particles, provided that the sedimentation is sufficiently fast to avoid any possible crystallization. Future studies in which sedimentation is slowed down by many orders of magnitude by fine-tuning the density of the solvent to approximate that of the colloids should allow the influence of crystallization on density and mechanical properties of the sediments to be detected.

In conclusion, our observations suggest that the structure of noncrystalline sediments may possibly be fully understood, based on the well-known microscopic structure of thermodynamically equilibrated fluids. This should possibly allow the jammed states formed in nonequilibrium particle systems, such as sand, to be characterized by comparison with our sediments, leading to a deeper understanding of noncrystalline solids.

ACKNOWLEDGMENTS. We thank Y. Roichman, Y. Shokef, M. Wyart, D. A. Weitz, Y. Rabin, M. Schwartz, and S. Torquato for fruitful discussions. We thank M. Shmilovitz (Tetra Sense Scientific Tools Ltd.) for assistance with the LUMiFuge experiments and P. Nanikashvili and D. Zitoun for experimental assistance. Part of the equipment used in this work was funded by the Kahn Foundation. This research is supported by Israel Science Foundation Grants 85/10 and 1668/10.

1. Bernal JD (1964) The Bakerian lecture, 1962. The structure of liquids. *Proc R Soc Lond A* 280:299–322.
2. Zhang Z, et al. (2009) Thermal vestige of the zero-temperature jamming transition. *Nature* 459(7244):230–233.
3. Wyart M (2005) On the rigidity of amorphous solids. *Ann. Phys. Fr.* 30(3):1–96.
4. Clusel M, Corwin EI, Siemens AON, Brujić J (2009) A 'granocentric' model for random packing of jammed emulsions. *Nature* 460(7255):611–615.
5. Kurita R, Weeks ER (2010) Experimental study of random-close-packed colloidal particles. *Phys Rev E Stat Nonlin Soft Matter Phys* 82(1 Pt 1):011403.
6. van Blaaderen A, Wiltzius P (1995) Real-space structure of colloidal hard-sphere glasses. *Science* 270(5239):1177–1179.
7. Jin Y, Makse HA (2010) A first-order transition defines the random close packing of hard spheres. *Physica A* 389(23):5362.
8. Stevenson JD, Schmalian J, Wolynes PG (2006) The shapes of cooperatively rearranging regions in glass-forming liquids. *Nat Phys* 2(4):268–274.
9. Parisi G, Zamponi F (2010) Mean-field theory of hard sphere glasses and jamming. *Rev Mod Phys* 82(1):789–845.
10. Kamien RD, Liu AJ (2007) Why is random close packing reproducible? *Phys Rev Lett* 99(15):155501.
11. Torquato S, Stillinger FH (2010) Jammed hard-particle packings: From Kepler and Bernal and beyond. *Rev Mod Phys* 82(3):2633–2671.
12. Jerkins M, et al. (2008) Onset of mechanical stability in random packings of frictional spheres. *Phys Rev Lett* 101(1):018301.
13. Onoda GY, Liniger EG (1990) Random loose packings of uniform spheres and the dilatancy onset. *Phys Rev Lett* 64(22):2727–2730.
14. Farrell GR, Martini KM, Menon N (2010) Loose packings of frictional spheres. *Soft Matter* 6(13):2925–2930.
15. Chaudhuri P, Berthier L, Sastry S (2010) Jamming transitions in amorphous packings of frictionless spheres occur over a continuous range of volume fractions. *Phys Rev Lett* 104(16):165701.
16. Ciamarra MP, Coniglio A, de Candia A (2010) Disordered jammed packings of frictionless spheres. *Soft Matter* 6(13):2975–2981.
17. Weitz DA (2004) PHYSICS. Packing in the spheres. *Science* 303(5660):968–969.
18. Umbanhowar PB, Goldman DI (2006) Low density fragile states in cohesive powders. *Am J Phys* 74(8):720–721.
19. Torquato S, Truskett TM, Debenedetti PG (2000) Is random close packing of spheres well defined? *Phys Rev Lett* 84(10):2064–2067.
20. Hansen J-P, McDonald IR (2006) *Theory of Simple Liquids* (Elsevier, New York).
21. Singer F, Singer SS (1971) *Industrial Ceramics* (Chapman and Hall, New York).
22. Cohen AP, Janai E, Mogilko E, Schofield AB, Sloutskin E (2011) Fluid suspensions of colloidal ellipsoids: Direct structural measurements. *Phys Rev Lett* 107(23):238301.
23. Cheng Z, Chaikin PM, Zhu J, Russel WB, Meyer WV (2002) Crystallization kinetics of hard spheres in microgravity in the coexistence regime: Interactions between growing crystallites. *Phys Rev Lett* 88(1):015501.
24. Bryant G, et al. (2002) How hard is a colloidal "hard-sphere" interaction? *Phys Rev E Stat Nonlin Soft Matter Phys* 66(6 Pt 1):060501–060504.
25. Poon WCK, Weeks ER, Royall CP (2012) On measuring colloidal volume fraction. *Soft Matter* 8(1):21–30.
26. Segrè PN, Liu F, Umbanhowar P, Weitz DA (2001) An effective gravitational temperature for sedimentation. *Nature* 409(6820):594–597.
27. Ziemann O, Krauser J, Zamzow PE, Daum W (2008) POF Handbook: Optical short range transmission systems, 2nd Ed. (Springer-Verlag, Berlin).
28. Blumenfeld R, Edwards SF, Ball RC (2005) Granular matter and the marginal rigidity state. *J Phys Condens Matter* 17(24):S2481–S2487.
29. Silbert LE, Ertaş D, Grest GS, Halsey TC, Levine D (2002) Geometry of frictionless and frictional sphere packings. *Phys Rev E Stat Nonlin Soft Matter Phys* 65(3 Pt 1):031304.
30. Schröter M, Goldman DI, Swinney HL (2005) Stationary state volume fluctuations in a granular medium. *Phys Rev E Stat Nonlin Soft Matter Phys* 71(3 Pt 1):030301.
31. Blum J, Schräpler R (2004) Structure and mechanical properties of high-porosity macroscopic agglomerates formed by random ballistic deposition. *Phys Rev Lett* 93(11):115503.
32. Silbert LE (2010) Jamming of frictional spheres and random loose packing. *Soft Matter* 6(13):2918–2924.
33. Ruiz-Montero MJ, Frenkel D, Frenkel D; ten Wolde PR (1995) Numerical evidence for bcc ordering at the surface of a critical fcc nucleus. *Phys Rev Lett* 75(14):2714–2717.
34. Gasser U, Weeks ER, Schofield A, Pusey PN, Weitz DA (2001) Real-space imaging of nucleation and growth in colloidal crystallization. *Science* 292(5515):258–262.
35. Shokef Y, Liu AJ (2010) Jamming mechanisms and density dependence in a kinetically constrained model. *Europhys Lett* 90(2):26005.
36. Schröter M, Nägle S, Radin C, Swinney HL (2007) Phase transition in a static granular system. *Europhys Lett* 78(4):44004.
37. Rubinstein SM, et al. (2011) Slip sequences in laboratory experiments resulting from inhomogeneous shear as analogs of earthquakes associated with a fault edge. *Pure Appl Geophys* 168(12):2151–2166.

Supporting Information

Liber et al. 10.1073/pnas.1214945110

Confocal Measurements

Confocal studies were carried out using a laser-scanning Nikon A1R setup in galvanometric scanning mode. The imaging was done with a 100× oil-immersion objective, with the voxel size set to 0.124 × 0.124 × 0.3 μm. For confocal imaging, the solvent was replaced by a (18:82, by volume) mixture of tetrahydronaphthalene (99%; Sigma-Aldrich) and *cis*-decahydronaphthalene (≥98%; Fluka) to match the refractive index of our colloids; this minimizes light scattering, to allow confocal imaging deep in the bulk of the sample. The fluid samples were then loaded into squared Vitrocom capillaries (0.6 × 0.6 × 50 mm) and centrifuged (with the capillaries supported by thick glass slides) to form solid sediments. Particle positions in three dimensions were extracted by a common particle tracking algorithm, corrected so as to avoid any rotationally-anisotropic convolution masks (1).

To confirm that the size of the particles does not change with the addition of tetrahydronaphthalene (THN), we performed a series of dynamic light scattering (DLS) measurements. The size of the particles, initially in decahydronaphthalene (DHN), was measured. Then the particles were transferred to pure THN and their size was tracked for a period of 1 wk. We note that the particles used for confocal measurements did not spend longer than several days within the THN-containing mixture, where the concentration of THN was also only 18% (by volume) rather than 100%, which we used for the DLS particle size tests.

The DLS measurements are carried out with the commercial goniometer-based Photocor dynamic light scattering setup. The normalized intensity autocorrelation function $g^{(2)}(\tau) = \langle I(\tau)I(t+\tau)\rangle/\langle I(t)\rangle^2$ is measured as a function of the delay time τ, with $I(t)$ being the intensity of light scattered to an angle θ with respect to the incoming laser beam of wavelength $\lambda = 633$ nm. We show the representative $g^{(2)}(\tau) - 1$ data in Fig. S1*A*, fitted by the theoretical expression $g^{(2)}(\tau) = B + \beta exp(-2\Gamma\tau)$, where $\Gamma(\theta)$ is the decay rate of the DLS correlations, β is the contrast, and B is the background; notice the perfect fit with the experimental data. The polydispersity of our particles is very small, so no corrections for polydispersity are needed in fitting the $g^{(2)}(\tau)$ data (2). The fitted values of $\Gamma(\theta)$ are shown in Fig. S1*B* as a function of the wave-vector transfer squared $q^2 = (4\pi n\lambda^{-1}sin(\theta/2))^2$, where n is the refractive index of the solvent. We obtain the diffusion constant as $D = \Gamma/q^2$, which is the slope of the dashed line passing through the experimental data in Fig. S1*B*. Finally, the particle diameter $\sigma = 2r$ at a given time t is obtained from the Stokes–Einstein relation $D = k_BT/(6\pi r\eta_s)$, where r is the radius of the particles and η_s is the viscosity of the solvent. Note that the diameter of the particles is the same, within error, in both pure DHN and THN (see Fig. S1*C*); moreover, the size of the particles does not change in pure THN over a course of 1 wk, at least. This indicates that the addition of THN to the samples, needed to improve the matching of refractive indices between the solvent and the colloids for confocal microscopy, does not induce other significant changes in these samples.

Transmission Profiles

To follow the position of the sedimentation front in real motion, as in Fig. 1, we collect light transmission profiles $I(x')$ along the sample, at different times t during the centrifugation process. Several typical profiles are shown in Fig. S2, where x' is the distance from the bottom of the sample. The data are normalized by the transmission I_0, which is measured with the same setup, with the sample being removed. A drop in transmission, clearly visible in all of the profiles, is associated with the front position, separating the highly transparent supernatant (at high x') from the colloidal suspension (at low x'), which is almost completely opaque at our wavelength of 870 nm. Note the very sharp boundary in the transmission profiles, separating the pure solvent and the dense suspension; such sharp boundaries, which do not broaden in time, are typical for highly monodisperse colloidal samples (3). Initially, front position changes linearly in time, with the front velocity being related to φ_0, as discussed in the main text. Later, when the sediment is fully formed and no particles remain in the fluid suspension, the front position is constant in time.

The corresponding full set of $I(x', t)$ data is shown in Fig. S3 for $\varphi = 0.35$. At early centrifugation times $t/t_D < 5$ the suspension is still homogeneous for $x' < 0.9L_0$. Thus, the light transmission profiles through this sample are flat (for $x' < 0.9L_0$) and the transmission is very low everywhere, about 10%. Later, as the particles move along $\vec{a}$, no particles are left in the high-x' part of the sample; the light transmission through this part of the sample is that of the pure solvent, ∼90%. The thickness of the colloid-free region at low x increases with the centrifugation time for $t/t_D < 20$, in this sample where $\varphi_0 = 0.35$. By $t/t_D \approx 20$, all particles have already found their way from the fluid suspension into the solid sediment. Thus, the particle concentration profile stays constant, as indicated by the light transmission profiles in Fig. S3, which are time-independent for $t/t_D > 20$.

Frictional Arrest of Rotational Diffusion

We confirm the presence of significant friction in our sediments by means of a direct experiment, reminiscent of the well-known fluorescence recovery after photobleaching technique (4). We bleach a line through our sample, using the 488-nm laser line of our Nikon A1R confocal microscopy setup. The width of the bleached line is smaller than the diameter of our particles; thus, most particles in the immediate vicinity of this bleached line have part of their perimeter appearing dark (invisible for confocal microscopy), as shown in Fig. S4. In our fluid suspensions, the particles rapidly rotate, such that their dark part moves in all directions. This, as also the translational motion of the particles, makes the dark bleached line disappear within seconds. The typical time for Brownian rotation of our particles in a pure solvent is $\tau_\theta = (2D_\theta)^{-1} = 12.8$ s, where $D_\theta = k_BT/(\pi\eta_s\sigma^3)$ is the rotational diffusion constant of our spheres. In colloidal sediments, the bleached region does not change and the particles do not rotate over a time scale of $100\tau_\theta$ (20 min), at least. This indicates that tangential friction forces between the particles are significant, arresting all Brownian rotation of the colloids. This conclusion is further supported by the comparison of our $\varphi_j(\varphi_0)$ data with computer simulations (discussed in the main text), where the number of contacts per particle within the sediment is obtained as $Z \approx 4$, corresponding to the isostatic conditions in systems of nonslipping particles.

Computer Simulations of Sedimentation

In our computer simulations, we first prepare a fluid of simple hard spheres at different volume fractions. To confirm that the system has reached thermodynamic equilibrium, we compare the $g(r)$ of the simulated system to the theoretical predictions, using the Percus–Yevick approximation (5); a perfect match between these two datasets is obtained for all φ_0. Initially, the boundary conditions are chosen to be periodic, in all of the three dimensions. The number of particles N was chosen to be between 4×10^3 and 4×10^5. The xy dimensions of the cell ($L \times L$) were either 10×10 or 30×30 (in σ units), whereas the size of the simulation cell in

z-direction was larger, determined by φ_0 and N; the results do not significantly depend on either N or L in our range of these values.

To prepare a sediment out of this simulated fluid, we let the particles fall, one by one, in the $-z$ direction. The particles that have lower z values fall first. A particle stops falling when it either has a sufficient number of supports Z_s from particles that already belong to the sediment or when it reaches $z = 0$. A contact between particles is established when the separation between their centers is below 1.005 (in σ units). We have carried out simulations with the number of supports per particle Z_s being chosen as either 1, 2, or 3; thus, the total number of contacts per particle Z was ~2, 4, or 6 (Fig. 4).

For $Z_s > 1$, when a falling particle forms its first contact with a particle from the sediment, it slides down along the circumference of this particle. Then it either falls further down or establishes a contact with an additional particle. For $Z_s = 2$, once this additional contact is established, the particle stops; this particle is then considered to belong to the sediment (Movie S1). For $Z_s = 3$, when the second contact is established, the particle continues to move along the surface of both of its supporting particles. Then it either falls further down or establishes its third contact with the sediment.

To obtain the volume fraction of the spheres within the simulated sediments, we measure the height of the sediment z_0 by fitting the density profile $\rho(z)$ with $0.5\rho_0[1 - erf(z - z_0)]$, where the bulk density ρ_0 and z_0 are tunable parameters. Then, the total volume of the N spheres is divided by z_0L^2 to obtain φ_j. The density profiles along the sediments $\rho(z)$ are typically perfectly flat, except for a couple of particle monolayers at the bottom ($z = 0$). The exclusion of the bottom monolayers from this calculation does not significantly change the result.

To confirm the validity of our φ_j, we carry out Voronoi tesselation of the sample (6). The hard volume of a sphere, divided by the volume of the corresponding Voronoi cell, yields the local volume fraction φ_{loc}. The probability to obtain a certain value of a local volume fraction $P(\varphi_{loc})$ is then calculated. The peak positions of these distributions coincide, within statistical error, with the φ_j values obtained from the heights of the sediments; this further proves the validity of our simulated φ_j values.

To further investigate the structure of the simulated sediments, we plot the distribution of the number of contacts per particle Z in a simulated sample (Fig. S5*A*). The distribution is described very well by a Gaussian function peaking at $Z = 4$, which is the average number of contacts per particle; some particles support fewer (or more) than two particles, depending on the local structure of the sediment, which results into a rather wide distribution of Z about its average value.

The experimental determination of contacts within the sediment is a highly challenging task (7). Therefore, to further test the validity of our simulations, we measure the number of nearest neighbors Z_{NN}, both in the simulated and in the experimental solid sediments. Nearest neighbors are defined by their spatial separation's being lower than the cutoff length $r_c = 1.3\sigma$, which roughly corresponds to the first minimum of the $g(r)$. To remove the explicit dependence of Z_{NN} on the particle density, we normalize these values by the coordination number Z_{NN}^{IG} in the ideal gas, at the same number density. The resulting distribution of $\zeta = Z_{NN}/Z_{NN}^{IG}$ for sediments prepared from a fluid suspension at $\varphi_0 = 0.27$ is shown in Fig. S5*B*; note the excellent agreement between the simulated and the experimental distributions. Further, we follow the variation in the peak position of $P(\zeta)$ for sediments prepared from fluids of different φ_0 (Fig. S5*C*). Again, a very good agreement between simulation and experiment is observed, suggesting that our simplified simulations catch the most important physical aspects of the sedimentation process.

1. Lu PJ, Sims PA, Oki H, Macarthur JB, Weitz DA (2007) Target-locking acquisition with real-time confocal (TARC) microscopy. *Opt Express* 15(14):8702–8712.
2. Frisken BJ (2001) Revisiting the method of cumulants for the analysis of dynamic light-scattering data. *Appl Opt* 40(24):4087–4091.
3. Detloff T, Sobisch T, Lerche D (2007) Particle size distribution by space or time dependent extinction profiles obtained by analytical centrifugation (concentrated systems). *Powder Technol* 174:50–55.
4. Axelrod D, Koppel DE, Schlessinger J, Elson E, Webb WW (1976) Mobility measurement by analysis of fluorescence photobleaching recovery kinetics. *Biophys J* 16(9):1055–1069.
5. Percus JK, Yevick GJ (1958) Analysis of classical statistical mechanics by means of collective coordinates. *Phys Rev* 110(1):1–13.
6. Barber CB, Dobkin DP, Huhdanpaa H (1996) The quickhull algorithm for convex hulls. *ACM Trans Math Softw* 22(4):469–483, www.qhull.org.
7. Jenkins MC, Haw MD, Barker GC, Poon WCK, Egelhaaf SU (2011) Finding bridges in packings of colloidal spheres. *Soft Matter* 7(2):684–690.

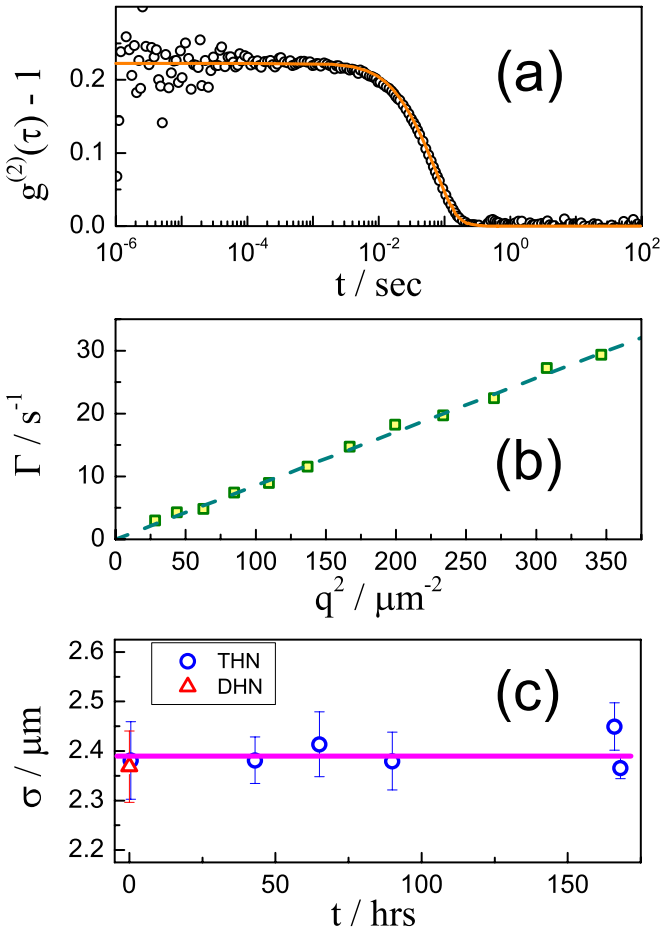

Fig. S1. (*A*) DLS autocorrelation data (symbols), taken at a constant scattering angle $\theta = 35°$, 1 d after the transfer of our particles to a pure THN. The solid curve is the theoretical fit. (*B*) The decay rates Γ, as a function of the wave-vector transfer squared q^2, taken 1 d after the transfer to THN. The dashed line is the fit to experimental data (squares). (*C*) The size of the particles in pure DHN (triangle) and in THN (circles). Note that no swelling or contraction of our particles is observed in pure THN over the course of 1 wk, at least.

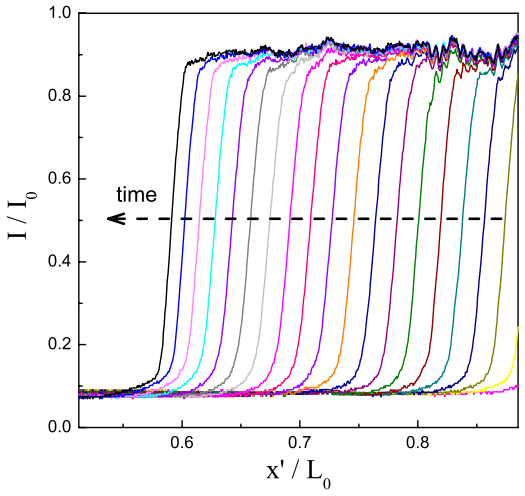

Fig. S2. Typical optical transmission profiles along the sample, obtained at different centrifugation times. Time difference between subsequent profiles is 10 s. The volume fraction of the particles in the fluid suspension is $\varphi_0 = 0.35$, the centrifugal acceleration is 1,170*g*, and L_0 is the initial height of the sample (Fig. 1 *Inset*). The front position, which is clearly visible, moves roughly linearly in time, such that the profiles are equally spaced. A slight slowdown of the front velocity is observed at late centrifugation times. Then the front velocity decays abruptly to zero (Fig. S3 and Fig. 1), as the sediment is fully formed. The optical transmission through the fluid suspension is below the background level of our setup. Thus, these very low transmission levels do not allow the fluid suspensions to be distinguished from the solid sediments.

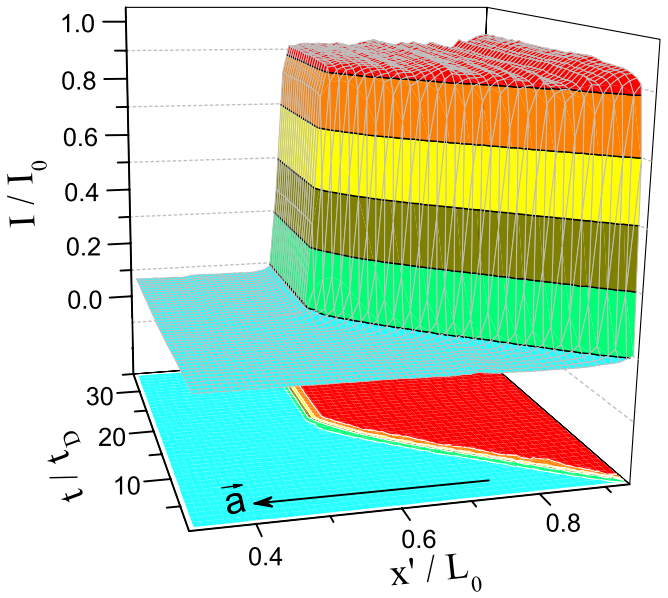

Fig. S3. The transmission profiles through a typical sample ($\varphi_0 = 0.35$, $a = 1{,}170g$). The projection of the color map onto the $x' - t$ plane is shown at the bottom. $\vec{a}$ is the centrifugal acceleration. $t_D = 12.8$ s is the self-diffusion time of an individual colloid in a pure solvent. The position of the sharp boundary between the colloid-free solvent and the sediment changes linearly in time for $t/t_D < 20$; then, the position is unchanged as the sediment is fully formed. For a given time t, the position at which the transmission is 50% (intermediate between that of the pure solvent and that of the suspension) is denoted by x, yielding the $x(t)$ dependencies in Fig. 1.

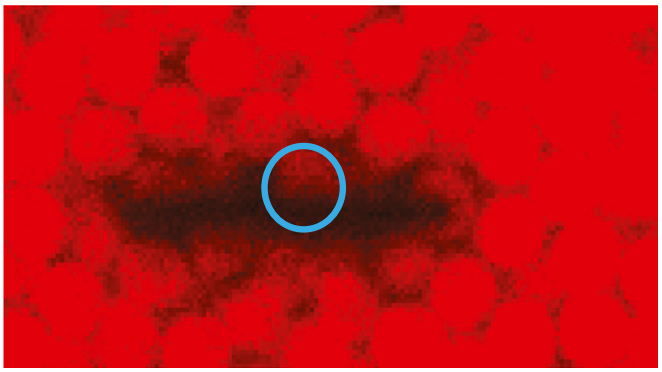

Fig. S4. We bleach a black line through one of our sediments. Most particles in the center of the image have one of their sides bleached, such that only half of the particle is visible by fluorescent microscopy. One such particle is circled in blue. In absence of friction, the black side of the particle would move as the particle undergoes Brownian rotational motion. The fact that no rotations are observed on a time scale of $100\tau_\theta$ indicates that the friction between our colloids is significant.

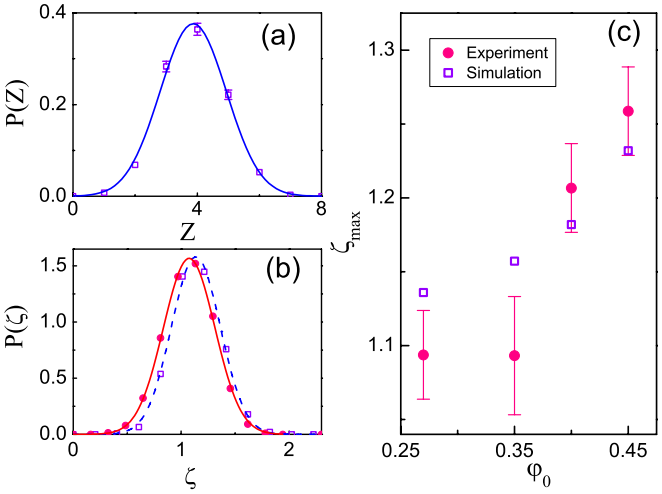

Fig. S5. (*A*) Distribution of contacts per particle in a simulated sediment, prepared from a fluid at $\varphi_0 = 0.27$. Note the significant width of the distribution. (*B*) The distribution of coordination numbers per particle in the sediments, as obtained in experiment (solid circles) and in the simulation (open squares). The coordination numbers are normalized by the average ones in the ideal gas at the same number density. Note the good agreement between experiment and simulation for these sediments, prepared from a fluid at $\varphi_0 = 0.27$. (*C*) The variation in the peak position of $P(\zeta)$ as a function of the φ_0 of the initial fluid suspension, from which the solid sediment is prepared. Again, a very good agreement between simulation and experiment is observed. The error bars are due to the variation between different samples.

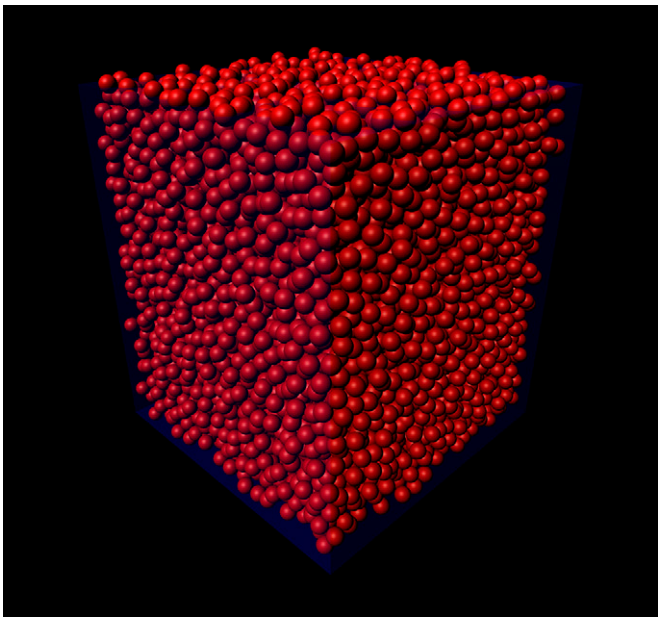

Movie S1. The simulated sedimentation of colloidal spheres. In this animation, each particle is arrested once it meets two supports, as described in *Supporting Information* and in the main text. Periodic boundary conditions are applied.

Movie S1